

Preliminary investigations of a potential optics system for wide-band X-ray telescopes

Liqiang Qi¹ , Tianxiang Chen¹, Zhengwei Li^{1*} , Qianqing Yin¹ , Congzhan Liu¹,
Weichun Jiang¹, Lin Li²

¹Key Laboratory of Particle Astrophysics, Institute of High Energy Physics, Chinese Academy of Sciences, Beijing 100049, China

²College of Mathematics and Physics, Beijing University of Chemical Technology, Beijing 100029, China

*Correspondence: lizw@ihep.ac.cn

Received: September 10, 2024; Accepted: November 6, 2024; Published Online: November 12, 2024; <https://doi.org/10.61977/ati2024051>; <https://cstr.cn/32083.14.ati2024051>

© 2024 Editorial Office of Astronomical Techniques and Instruments, Yunnan Observatories, Chinese Academy of Sciences. This is an open access article under the CC BY 4.0 license (<http://creativecommons.org/licenses/by/4.0/>)

Citation: Qi, L. Q., Chen, T. X., Li, Z. W., et al. 2024. Preliminary investigations of a potential optics system for wideband X-ray telescopes. *Astronomical Techniques and Instruments*, **1**(6): 335–344. <https://doi.org/10.61977/ati2024051>.

Abstract: We present preliminary investigations of a potential optics system for wideband X-ray telescopes. The optical design adopts the conical approximation of the Wolter-I configuration and a combination of multilayer coatings and silicon pore optics. The total number of mirror modules is 79, distributed in 8 rows with the radii at the intersection plane between 250 mm and 500 mm. The optimization of the total effective area using the figure of merits method suggests that the focal length is 30 m and the mirror coating is a combination of the W/Si and Pt/C multilayers. This fulfills the on-axis effective area requirements of 2000 cm² at 10 keV and 300 cm² at 60 keV and provides a broad energy response between 3 keV and 78.4 keV. With the current geometry and coating compositions, we implement a mass modeling of the telescope in Geant4 to predict mirror performances via the ray-tracing algorithm, including the angular resolution and effective area. With the presumed metrological data as input, this can provide precision and finishing requirements for the manufacture of optics. This work demonstrates the feasibility of combining multilayer coatings and silicon pore optics for potential use in wideband X-ray telescopes and advances the development and progress of such missions.

Keywords: Depth-graded multilayer; Silicon pore optics; Wideband X-ray telescope; High-energy astrophysics

1. INTRODUCTION

In X-ray astronomy, Wolter-I optics are widely used to focus and image photons at shallow grazing-incidence angles because the real part of the complex refractive index of materials above a few tens of eV is slightly smaller than unity^[1]. Below 10 keV, the single layer or bilayer coating of materials made from elements with a high atomic number (i.e., high-Z materials) is usually used to fulfill the condition of total internal reflection, such as in the Chandra X-ray Observatory^[2], XMM-Newton^[3], eROSITA^[4]. The critical angle of total internal reflection is inversely proportional to the X-ray energy. Above 10 keV, it becomes very small with a single or bilayer coating, such that a large aperture and a long focal length are necessary to achieve scientific goals. Multilayer coatings were proposed to increase reflectivities above 10 keV with grazing-incidence angles larger than the critical angles of a single or bilayer coating^[5]. It is based on the

principle of constructive interference by stacking a series of bilayers composed of high-Z and low-Z materials. The thickness of the bilayers varies systematically in the multilayer stack, creating multilayers graded by depth that yield a relatively smooth distribution of reflectivities over a broad energy range. The Nuclear Spectroscopic Telescope Array (NuSTAR, launched in 2012) adopts a depth-graded multilayer coating in the Wolter-I type mirror, used to observe soft and hard X-rays in the energy range of 5–80 keV^[6]. The optics consist of a large number of thin, slumped glasses with 10 different coatings to construct a smooth effective area curve^[7].

Though the existing technologies such as slumped glass, nickel electroforming shell, or thin foil, can be used to construct the optics system, the weight and cost increases dramatically to meet the scientific requirements, e.g. the on-axis effective area of 2000 cm² at 10 keV and 300 cm² at 60 keV, and angular resolution of 30'' at 30 keV. Instead, the technique of the Silicon Pore Optics

(SPO) is a highly promising option to construct the optics system. SPO is adopted in the Advanced Telescope for High ENergy Astrophysics (ATHENA) mission^[8] to manufacture lightweight, stiff, and precise soft X-ray focusing telescopes with a large effective area and good angular resolution. The SPO technique stacks a series of wedged and grooved silicon plates with the required curvatures in the azimuthal direction and conical, parabolic, or hyperbolic profiles in the optical direction^[9]. The stacking is directly bonded by covalent interactions between smooth silicon plates without requiring any epoxy or glue. The SPO technique relies on the commercial semiconductor industry, allowing for an efficient production of high-quality and precision segmented mirror modules. Our aim is to investigate X-ray focusing optics systems for potential use in wideband X-ray telescopes constructed with a combination of multilayer coatings and SPO, aiming to fulfill the stringent scientific requirements of effective area and angular resolution.

The optics design is crucial in space missions. It ensures the focusing telescope will meet the scientific requirements accurately and optimizes mirror performance by maximizing effective area, minimizing focal length, and improving angular resolution. In Section 2, the procedure and results of the optical design are presented to fulfill the on-axis effective area requirements. Additionally, the mission development requires a simulation of the achievable performance of the complete optics with metrological data. The predicted mirror performance can be compared with X-ray calibration results, which helps in understanding the measurements. It can also be used to derive the error budget for the multilayer coating, SPO manufacturing, and alignment. In Section 3, a ray-tracing model, using surface metrological data, is implemented within the simulation framework of Geant4^[10]. We present details of the implementation and predicted performances within assumptions, including angular resolution and effective area. Finally, summaries are given in Section 4.

2. OPTICS DESIGN

2.1. Reflectivity of Multilayer

The aim of this work is not to develop full-featured software to calculate the X-ray reflectivity of multilayer structures under various situations. Instead, an efficient and portable module is required for a purely rough surface and interface, which is callable in the later-on effective area calculation of the optics system. The theoretical computation of the X-ray reflectivity follows the Névot-Croce formalism^[11] and Parratt's recursive formula^[12]. It is based on the Fresnel equations with modifications according to surface and interface imperfections. In the case of a multilayer stack containing N layers (where 1 is the top-most layer and N is the bottom-most layer), the calculation starts from the net reflection of the bottom-most

layer^[12-14],

$$r_N = \frac{r_{(N-1)N} + r_{NS} e^{2i\beta_N}}{1 + r_{(N-1)N} r_{NS} e^{2i\beta_N}}, \quad (1)$$

where r_N is the net reflection of N^{th} layer, $r_{(N-1)N}$ is the Fresnel reflection coefficient of the interface between the $(N-1)^{\text{th}}$ and N^{th} layer, r_{NS} is the Fresnel reflection coefficient of the interface between the N^{th} layer and substrate, and $\beta_N = 2\pi d_N n_N \sin \theta_N / \lambda$ is the phase difference (in which d_N is the layer thickness, n_N is the refraction index, θ_N is the refracted angle of N^{th} layer, and λ is the X-ray wavelength). The net reflection of the multilayer stack is then obtained recursively from the bottom-most layer to the top-most layer using the relationships^[12-14]

$$r_{N-1} = \frac{r_{(N-2)(N-1)} + r_N e^{2i\beta_{N-1}}}{1 + r_{(N-2)(N-1)} r_N e^{2i\beta_{N-1}}}, \quad (2)$$

and

$$r_1 = \frac{r_{01} + r_2 e^{2i\beta_1}}{1 + r_{01} r_2 e^{2i\beta_1}}, \quad (3)$$

where 0 refers to the ambient material. To account for surface and interface imperfections, the Fresnel reflection coefficients in Equations (1), (2), and (3) are modified with the Névot-Croce correction factor^[11]. In the case of a purely rough surface and interface, the correction factor that results from a Gaussian distribution of surface irregularities is^[13]

$$e^{-(4\pi \sqrt{\sin^2 \theta_{N-1} \sin^2 \theta_N / \lambda^2} \sigma^2 / 2)}, \quad (4)$$

where σ is the root mean-square-roughness of the surface or the interface. The refraction index in this module directly uses the database of the IMD software, which is widely used in the design and characterization of X-ray mirrors^[13].

We validate the accuracy of the reflectivity calculation in this module using the IMD software. The reflectivities of three types of layered structures are calculated in the validation, including single-layer, constant period multilayer, and depth-graded multilayer (with all grazing-incidence angles set to 0.2°). In the first case, a single tungsten layer coated on a silicon substrate has a thickness of 1000 Å with a surface roughness of 5 Å. Fine structures caused by tungsten atoms can be seen in the reflectivity curve (Fig. 1A). In the second case, a constant period multilayer has 100 bilayers of tungsten and silicon with a constant period of 40 Å. The surface and interface roughness is 5 Å. The ratio between the thickness of the high-Z material and that of the bilayer, denoted Γ , is 1/3. Similar to Bragg diffraction in a crystal lattice, reflectivity is enhanced in a very narrow energy band around 47 keV (Fig. 1B). In the third case of a depth-graded multilayer, the thickness of W/Si bilayers d_i varies continuously, following a conventional power-law distribution^[15] given by

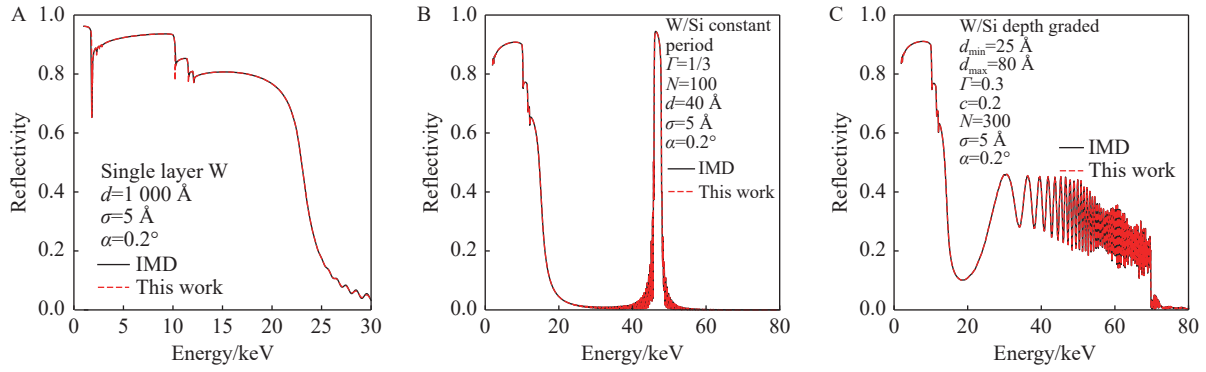


Fig. 1. Comparison of the reflectivity calculation between IMD and this work, in the case of a single layer (A), constant period multilayer (B) and depth-graded multilayer (C). The detailed coating parameters are included in the legends.

$$d_i = \frac{a}{(b+i)^c}, i \in [1, N], \quad (5)$$

$$a = d_{\min}(b+N)^c, \quad (6)$$

$$b = \frac{1-Nk}{k-1}, \quad (7)$$

and

$$k = \left(\frac{d_{\min}}{d_{\max}} \right)^{\frac{1}{c}}, \quad (8)$$

where N is the total number of bilayers, d_{\min} and d_{\max} are the thickness of the bottom-most ($i = N$) and top-most bilayer ($i = 1$), respectively. Due to the continuous thickness variation of bilayers, the reflectivity has a broad energy response above 30 keV compared to that of the constant-period multilayer (Fig. 1C), which is usually more suitable for practical use in an X-ray focusing telescope. Overall, the calculation results of the module in this work are in good agreement with that of IMD in terms of peak positions and amplitudes. It ensures the accuracy and reliability of the later effective area calculation of the optics system.

2.2. Geometric Collection Area of SPO

A schematic view of a radial section of a pore used in SPO is plotted in Fig. 2A. The plate pair (No. 1) con-

sists of the primary segment with length L_1 and the secondary segment with length L_2 . Both segments have gaps separating them from the intersection plane, with distances of D_1 and D_2 , respectively. The radius of the intersection plane is R_0 . In this design, the primary and secondary segments have the same length, gap, and intersection plane, i.e. $L_1 = L_2 = L$, $D_1 = D_2 = D$. A perspective view of one SPO mirror module is shown in Fig. 2B. The inset shows a pore along the optical axis, with the azimuthal width w , radial height h , rib width t , and membrane thickness τ . Similar to the nested configuration of conventional Wolter-I type mirrors, the next shell (No. 2) is placed inward with a distance of $h = (L-D)\tan\alpha_0$, where α_0 is the grazing-incidence angle at the intersection plane for an on-axis source at infinity. The primary and secondary segments in each SPO mirror module consist of 35 silicon plates. The parameters of the geometry used in this work are summarized in Table 1.

Here, the analytical formula used by Spiga et al.^[16] under the conical approximation is used to calculate the effective area of a single pore A_{pore} as

$$A_{\text{pore}}(\lambda, \theta) = [w - 2L\theta|\sin\varphi|]_{\geq 0} [(L-D)\alpha_0 - 2\theta L|\cos\varphi|]_{\geq 0} \times r_\lambda(\alpha_1) r_\lambda(\alpha_2), \quad (9)$$

where λ is the wavelength of incident X-rays, θ is the off-axis angle, r is the reflectivity at a given wavelength

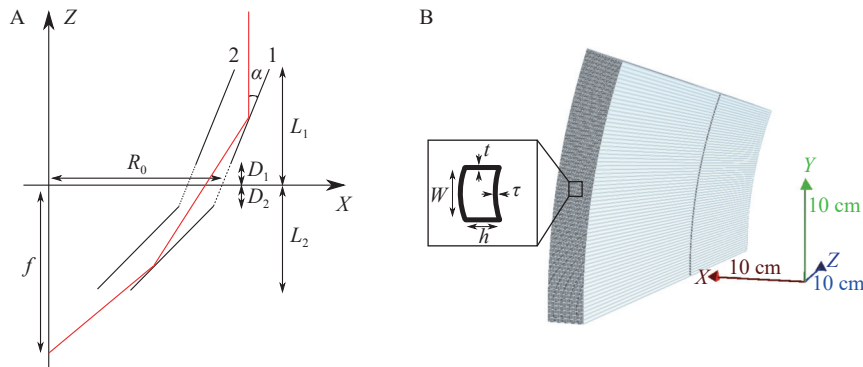


Fig. 2. Schematic view of a radial section of a pore used in SPO (A). Perspective view of one SPO mirror module with an inset showing a pore along the optical axis (B).

Table 1. Summary of the geometric parameters in SPO of this work

Parameter	L/mm	D/mm	w/mm	τ/mm	t/mm	h/mm	Number of plates in each stack
Value	202	2	2.4	0.15	0.6	$(L-D)\tan\alpha_0$	35

and grazing-incidence angle, and φ is the azimuthal angle of the pore, relative to that of the incident X-rays. α_1 and α_2 are the grazing-incidence angles for the primary and secondary segments, respectively, for a hypothetical astronomical source at infinite distance. These are functions of the off-axis angle θ and the azimuthal angle φ [16], determined as

$$\alpha_1 = \alpha_0 - \theta \cos \varphi, \quad (10)$$

and

$$\alpha_2 = \alpha_0 + \theta \cos \varphi. \quad (11)$$

When setting the reflectivities of r_λ to 1, Equation (9) can be used to find the geometric collection area of a single pore. The total geometric collection area of one SPO mirror module can be obtained by summing the contributions from all pores within it.

To validate the analytical formula to calculate the geometric collection area used in SPO, a ray-tracing calculation is performed using the Geant4 toolkit. Geant4 is widely used in X-ray astronomy to predict the performance of telescopes and systems of optics [17–20]. The details of the implementation of this toolkit can be found in Section 3. The geometric collection area of one SPO mirror module as a function of off-axis angle ($\varphi = 0^\circ$) is plotted in Fig. 3A. As the off-axis angle increases, the geometric collection area decreases much faster than that of soft X-ray focusing telescopes. This is primarily caused by the grazing-incidence angle α_0 being much smaller in hard X-ray optics. The second term in Equation (9) limits the

field of view (FOV), inducing a quick variation of the geometric collection area with the off-axis angle. The azimuthal dependence of the off-axis geometric collection area ($\theta = 2'$) is plotted in Fig. 3B. A single mirror module shows a strong dependence on the azimuthal angle. Overall, there is strong agreement between the analytical formula and ray-tracing calculation. The maximum deviation in azimuthal dependence is less than 3%, and the deviation of the integral over the azimuthal angles is less than 1%. The cross-validation between different methods allows the subsequent effective area calculation to directly use the analytical formula with higher computational speed. This also ensures the accuracy and reliability of the calculation.

2.3. Optimization of Total Effective Area

The optimization focuses on the total effective area of the telescope aiming to fulfill the requirements of 2000 cm² at 10 keV and 300 cm² at 60 keV. The maximum radius of the aperture is limited to approximately 500 mm. The minimum azimuthal curvature radius is limited to above approximately 250 mm due to the mechanical properties of silicon wafers. Given the fixed dimension of the aperture, a focal length of 23.94 m is required to keep the grazing-incidence angle of the telescope below 0.3°. When the focal length is 30 m, the grazing-incidence angles of the telescope range from 0.119° to 0.239°, which are similar to those of NuSTAR (between 0.077° and 0.270°) but in a narrower range. Due to the long focal length, the optics can use conical surfaces instead of parabolic/hyperbolic surfaces, i.e., the conical approximation to a Wolter-I design. To simplify the manu-

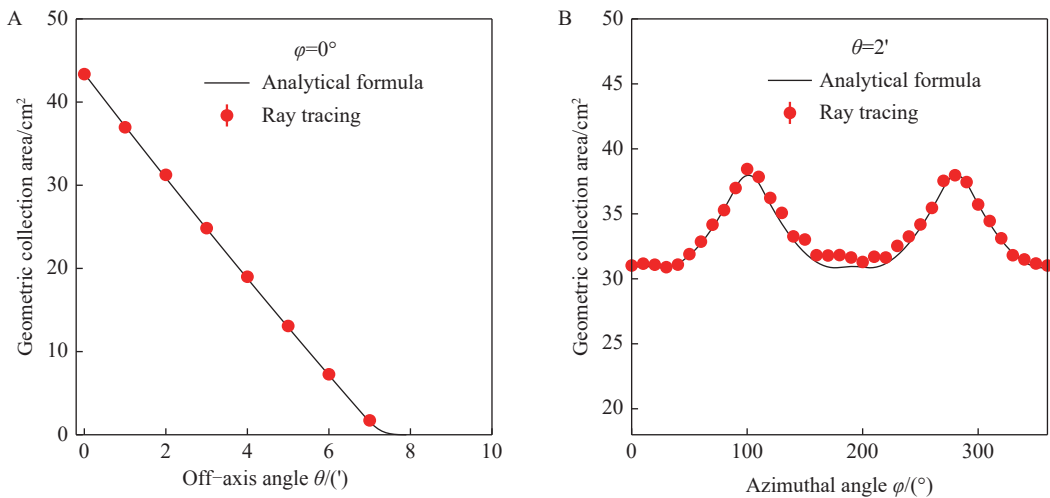


Fig. 3. Comparison of the geometric collection area calculation of one SPO mirror module between the analytical formula and ray tracing. The geometric parameters of this mirror module are the same as those in Table 1. R_0 of the outermost plate is 500 mm with a local length of 29 m. (A) shows a plot of the variation of the geometric collection area as a function of off-axis angle ($\varphi = 0^\circ$). (B) plots the variation as a function of azimuthal angle ($\theta = 2'$).

facturing process, the upper and lower conical section in each mirror module shares the same geometric dimensions used in the existing design, i.e., the parameters of L , D , w , τ , and t . The difference is that the spacing between each plate of the stack varies as a function of α_0 . In other words, the stacks of the SPO mirror modules in the inner rows become more densely nested. To leave adequate spacing between mirror modules in the radial and azimuthal directions for mounting, 79 modules can be placed in 8 rows with all previously mentioned constraints. A schematic view of the layout of 79 mirror modules is shown in Fig. 4 and Table 2, with a summary of

the parameters of the geometric configurations at three different focal lengths.

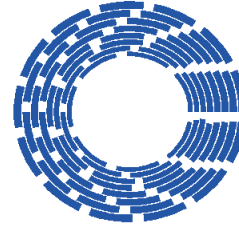


Fig. 4. Schematic view of the layout of 79 mirror modules.

Table 2. The geometric parameters at three different focal lengths

Focal length/m	Outermost R_0 per row/mm	Number of mirror modules per row
28	500, 460, 423, 388, 355, 324, 294, 267	13, 12, 11, 10, 9, 9, 8, 7
29	500, 461, 425, 390, 358, 327, 299, 271	13, 12, 11, 10, 9, 9, 8, 7
30	500, 462, 426, 393, 361, 331, 302, 276	13, 12, 11, 10, 9, 9, 8, 7

Since the grazing-incidence angle of the optics is within the angular range of NuSTAR, the NuSTAR coating compositions are adopted in this optics design, i.e., a depth-graded multilayer structure using W/Si and/or Pt/C bilayer materials. Given the geometric parameters of each mirror module and corresponding coatings, the effective area of the telescope can be analytically calculated by multiplying the projected geometric collection area, the reflectivities at different grazing-incidence angles, and X-ray energies. These two components are discussed and validated in previous sections. Optimization of the total effective area is then performed on the coating parameters of d_{\max} and c at different focal lengths (other coating parameters of d_{\max} , N , σ , Γ_{top} , and Γ_{stack} are fixed according to Christensen et al.^[7]). It follows the Figure of Merits (FOM) procedure to calculate the integral^[21],

$$FOM = \frac{\sum_{i=1}^N \int_{\theta_{\min}}^{\theta_{\max}} d\theta \int_{E_{\min}}^{E_{\max}} A_i(E, \theta) W_E(E) dE}{(\theta_{\max} - \theta_{\min})(E_{\max} - E_{\min}) < W_E >}, \quad (12)$$

where A_i is the effective area of i^{th} mirror module at the energy E and the off-axis angle θ , and W_E is the weighting function to control the shape of the effective area curve. A linear function is used as the weighting function to approximately equalize the importance of the effective area at 3 keV and at 60 keV. The optimization is performed using W/Si and Pt/C bilayer materials on each row of mirror modules. An example of the FOM distribution as a function of d_{\max} and c is shown in Fig. 5 and Table 3.

The total on-axis effective area curves of the optics are shown in Fig. 6 with W/Si and Pt/C bilayer materials at three different focal lengths. The energy bin size is 1 keV by default. The scientific requirements of the on-axis effective area are presented with orange solid lines, i.e., 2000 cm² at 10 keV and 300 cm² at 60 keV. As the

focal length increases, the effective area decreases at low X-ray energies and increases at high X-ray energies. This is primarily because when the focal length increases, the decrease in geometric collection area dominates in the total reflection regime, while the increase of reflectivities with shallower grazing-incidence angles dominates in the Bragg diffraction regime. The energy response of the W/Si multilayer is limited up to 69.5 keV due to the K-absorption edge of W and the energy response of the Pt/C multilayer is limited up to 78.4 keV due to the K-absorption edge of Pt. Similarly to NuSTAR, a combination of W/Si and Pt/C coatings leads to a relatively smooth distribution of the effective area up to 78.4 keV (Fig. 7A). It also suggests that a focal length of 30 m with the combined coatings is a good compromise to meet the scientific requirements of the on-axis effective area with a sustainable focal length, i.e., 2296 cm² at 3 keV and 354 cm² at 60 keV. In Fig. 7B, the on-axis effective area curve is plotted with a finer energy bin size of 0.1 keV. The observed zigzag shape is due to the atomic structures of W and Pt in the total reflection regime, and Bragg peak oscillations in the Bragg diffraction regime. To further smooth the dis-

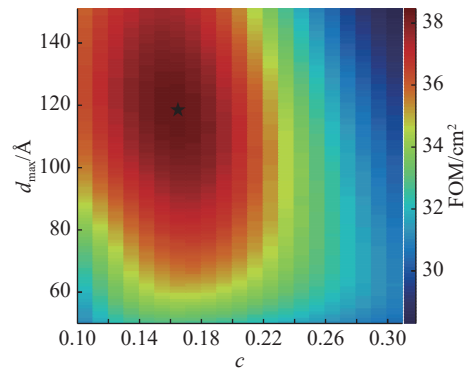


Fig. 5. FOM distribution as a function of coating parameter d_{\max} and c . The position with the largest FOM is marked with a star.

Table 3. The optimized coating parameters of each row at three different focal lengths

Coating	Focal length/m	d_{\max} per row/Å	c per row
W/Si	28	109, 116, 111, 97, 119, 119, 123, 115	0.19, 0.20, 0.21, 0.23, 0.23, 0.24, 0.25, 0.27
	29	105, 117, 132, 109, 118, 114, 117, 117	0.20, 0.20, 0.21, 0.23, 0.24, 0.25, 0.26, 0.27
	30	104, 111, 95, 109, 110, 123, 116, 118	0.20, 0.21, 0.22, 0.23, 0.24, 0.25, 0.26, 0.27
Pt/C	28	118, 118, 119, 122, 123, 121, 126, 130	0.16, 0.17, 0.18, 0.18, 0.19, 0.20, 0.21, 0.22
	29	118, 119, 119, 120, 123, 119, 127, 131	0.16, 0.17, 0.18, 0.19, 0.19, 0.21, 0.21, 0.22
	30	117, 120, 120, 120, 122, 129, 128, 129	0.17, 0.17, 0.18, 0.19, 0.20, 0.20, 0.22, 0.23

tribution, an extended optimization can be performed by tuning other coating parameters^[7], which is beyond the scope of this study. The combined coating compositions for the optics are summarized in Table 4.

3. PERFORMANCE PREDICTION

Geant4 provides a flexible and extensible framework for defining and constructing complex geometries^[10], which is suitable for SPO with hundreds of thousands of

geometries. Additionally, it has been used in previous work^[19, 20] to simulate the mirror performance of soft X-ray optics with nested Wolter-I configurations (created with Nickel electroforming using the shell replication technique), including the effective area, angular resolution, and polarimetric response. It uses the Mueller matrix of total internal reflection for a metallic mirror to track the Stokes parameters of reflected X-rays and detailed data on surface morphology to modify the interaction positions of X-rays on the optical surfaces and corresponding

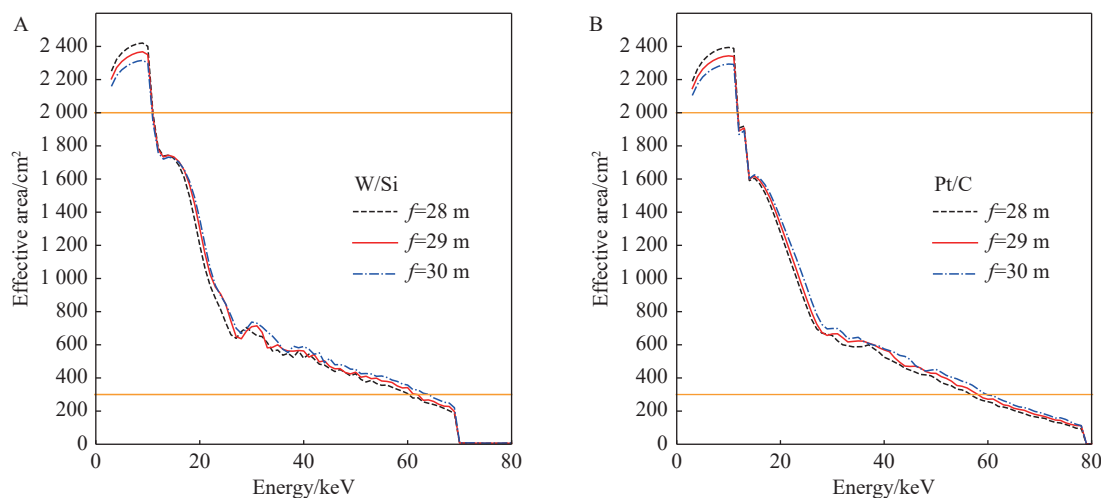


Fig. 6. Total on-axis effective area curve of the optics using W/Si (A) and Pt/C (B) bilayer materials at three different focal lengths. The energy bin size is 1 keV. The orange solid lines represent the scientific requirements of on-axis effective area of 2000 cm² at 10 keV and 300 cm² at 60 keV.

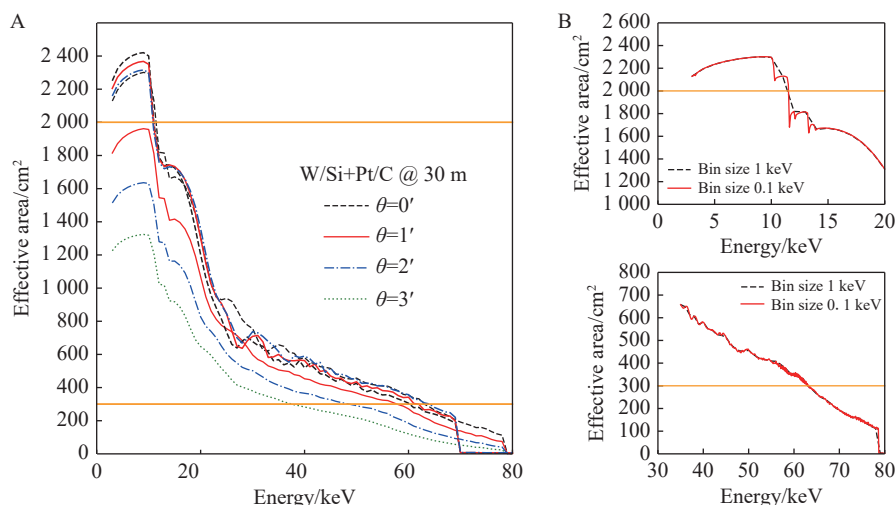


Fig. 7. Total effective area curve of the optics at different off-axis angles with the combined W/Si and Pt/C bilayer materials (A). The focal length is 30 m. Comparison of the on-axis effective area curves with different energy bin sizes (B). The red curve has a finer energy bin size of 0.1 keV.

Table 4. Summary of the coating compositions for the optics. Row 1 is the outermost ring and Row 8 is the innermost ring.

Row	$d_{\min}/\text{\AA}$	$d_{\max}/\text{\AA}$	N	c	$\sigma/\text{\AA}$	Γ_{stack}	Heavy	Light	Γ_{top}
1	25	104	291	0.20	4.3	0.38	W	Si	0.8
2	25	111	291	0.21	4.3	0.38	W	Si	0.8
3	29	120	145	0.18	4.5	0.45	Pt	C	0.7
4	29	120	145	0.19	4.5	0.45	Pt	C	0.7
5	29	122	145	0.20	4.5	0.45	Pt	C	0.7
6	29	129	145	0.20	4.5	0.45	Pt	C	0.7
7	29	128	145	0.22	4.5	0.45	Pt	C	0.7
8	29	129	145	0.23	4.5	0.45	Pt	C	0.7

surface normals. Here, the simulation framework is extended to hard X-ray optics with the combination of multilayer coating and SPO. However, since Bragg diffraction is the responsible physical mechanism in the high-energy region, the Mueller matrix of total internal reflection is not applicable. The polarimetric response is out of the scope of this paper, which instead focuses on mirror performance predictions of angular resolution and effective area using metrological data.

The ray-tracing algorithm is used to predict mirror performance because the aperture diffraction can be neglected above 0.5 keV and the angular resolution is usually dominated by low-frequency surface errors^[22]. The complex geometry of the optics is built by replicating each pore to complete the mirror modules. An illustration showing the mass modeling of the optics and the area of the focal plane detector is shown in Fig. 8. Each pore structure has four surfaces and only the coated surface (membrane) is considered to be reflective in this study, i.e., G4OpticalSurface of Geant4. We implement the low-energy physics of X-rays (i.e., the reflection and scattering of X-rays on the optical surfaces) as boundary processes, incorporating this into the standard physics list provided by Geant4^[10]. The measured low-frequency surface error, or a random surface error with a given distribution, is considered to simulate the angular resolution in soft X-ray optics^[19, 20]. This alters the surface normal vector at the interaction positions of X-rays on the deformed mirror surface. Additionally, the X-ray scattering effect caused by surface roughness at a microscopic scale becomes prominent in the case of hard X-ray optics. When the smooth surface condition is fulfilled, the intensity distribution of the scattered X-rays is proportional to the Power Spectral Density (PSD) of the surface according to first-order scattering theory^[23]. Therefore, it can also be implemented in the ray-tracing algorithm to sample the directions of the scattered X-rays.

3.1. Angular Resolution

The multilayer coating is used to increase the reflectivity of X-rays in the high-energy range. The number of layers can be up to 291 as is listed in Table 4. The roughness profile of the layer interfaces can be correlated, inducing pronounced peaks in the intensity distribution of the scattered X-rays^[16]. To account for possible correlation between interfaces in a stack of alternating N layers, a generalization of the scattered intensity distribution is pro-

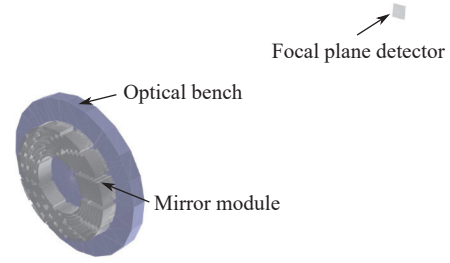


Fig. 8. Illustration of mass modeling of the optics with the area of the focal plane detector.

posed in Salmaso et al.^[24] as

$$\frac{1}{I_0} \frac{dI_s}{d\theta_s} = \frac{16\pi^2}{\lambda^3} \sin\theta_i \sin^2\theta_s \sqrt{R(\theta_s)R(\theta_i)} \left[\sum_{j=0}^N T_j^2 P_j(f) + 2 \sum_{j < m} (-1)^{j+m} C_{jm}(f) T_j T_m \cos(\alpha\Delta_{jm}) \right], \quad (13)$$

where I_0 is the incident beam intensity, I_s is the scattered beam intensity, θ_i is the grazing-incidence angle, θ_s is the off-surface scattering angle, R is the reflectivity of the interface between heavy and light materials, T_j is the amplitude of the electric field at the j^{th} interface, P_j is the PSD of the j^{th} interface, and f is the spatial frequency. For other parameters refer to Salmaso et al.^[24] for further information. A complete characterization of the multilayer structure requires surface topography, X-ray reflectivity, and X-ray scattering measurements^[25]. Currently, a deficit of metrological data prohibits proper input of the scattered intensity distribution into the calculation. Instead, an initial guess can neglect the correlation between interfaces and assume no evolution of PSD in the multilayer structure. It simplifies Equation (13) to

$$\frac{1}{I_0} \frac{dI_s}{d\theta_s} = \frac{16\pi^2}{\lambda^3} \sin\theta_i \sin^2\theta_s \sqrt{R(\theta_s)R(\theta_i)} P(f). \quad (14)$$

In this study, a power-law distribution of PSD with a spectral index of 1.8 and a micro-roughness of 0.5 nm is used as input for the calculation.

The geometric Encircled Energy Function (EEF), with an ideal surface profile at different off-axis angles, is shown in Fig. 9A. Two quantities are used to characterize the angular resolution, namely W50 (the diameter enclosing 50% of the collected photons) and W90 (the

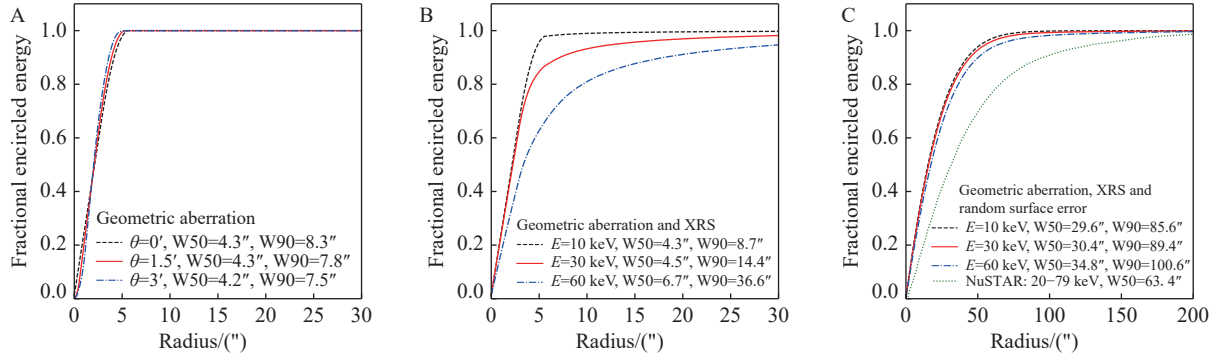


Fig. 9. Comparison of geometric EEFs at different off-axis angles (A). Comparison of EEFs at different X-ray energies, taking into account the XRS effect (B). Comparison of EEFs at different X-ray energies, taking into account the XRS effect and random low-frequency surface errors (C). The EEF of NuSTAR is also plotted in the right panel for comparison. The data are extracted from the NuSTAR Observatory Guide.

diameter enclosing 90% of the collected photons). W50 of the geometric EEF is a very small number of approximately 4", compared to the scientific requirements of 30" at 30 keV, due to the long focal length. It also varies insignificantly within the field of view. After the incorporation of the X-Ray Scattering (XRS) effect with a power-law PSD (Equation (14)), the quantity of W50 at 60 keV increases slightly to 6.7", while the quantity of W90 at 60 keV increases dramatically to 36.5" (Fig. 9B). This indicates that the input parameters of the PSD do not strongly degrade the angular resolution, which leaves an adequate margin of precision error for the low-frequency surface irregularities and alignment. By tuning the standard deviation in the Gaussian function ($\sigma \approx 13''$), the EEF induced by XRS and random low-frequency surface errors can be obtained with the quantity of W50 being $\approx 30''$ at 30 keV (Fig. 9C). An example of the on-axis point spread function induced by XRS and random low-frequency surface errors is shown in Fig. 10.

3.2. Effective Area

To simulate the effective area of the optics, a tabulated reflectivity as a function of energy and grazing-incidence angle for each coating recipe is pre-calculated according to the methods and the results described in Section 2.1. During the ray tracing process, the reflectivity at interaction positions on the optical surface is interpolated from the tabulated data.

The simulated on-axis effective area with an ideal surface profile is plotted in Fig. 11A, including the contributions from each row. Due to the differences in the grazing-incidence angle and the coating composition of each row, the characteristic Bragg peaks in the effective area curve counterbalance, forming a relatively smooth distribution overall. The total on-axis effective area is compared with that calculated from the analytical formula (see Section 2) with good observed agreement. The cross-validation of the effective area using different methods ensures the reliability of the calculation results. The evolution of effective area as a function of off-axis angle is plotted in Fig. 11B. Due to the large focal length and shallow grazing-incidence angles, the field of view of the optics,

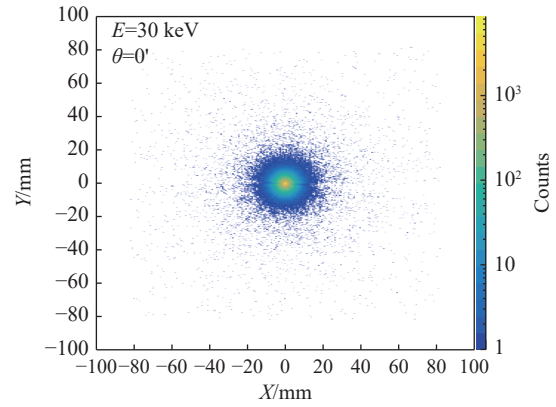


Fig. 10. On-axis point spread function accounting for the XRS effect and random low-frequency surface errors ($E = 30$ keV).

where the effective area drops to 50% of its maximum, is limited to approximately $3.64'$. The rapid variation of the effective area within the field of view demands a high pointing stability of the platform and a high alignment accuracy of the mirror modules. Additionally, the total effective area is re-calculated considering the XRS effect and random low-frequency surface errors (see Fig. 12). The effective area is decreased by 6% on average due to the variation of the grazing-incidence angles, but a smoother distribution of the effective area can be obtained, especially in the Bragg diffraction regime.

4. SUMMARIES

To design an optics system for wideband X-ray telescopes, we implement an efficient and portable module to calculate the reflectivities of multilayer structures, and validate it using IMD. Along with the analytical formula of the geometric collection area of SPO, the total effective area of the optics can be calculated. This allows the optimization of the coating parameters and focal length using FOM methods. The optimized optics design uses the conical approximation to the Wolter-I configuration with a focal length of 30 m. The total number of mirror modules is 79, distributed in 8 rows, and the radii of the intersection plane range from 250 mm to 500 mm. The mir-

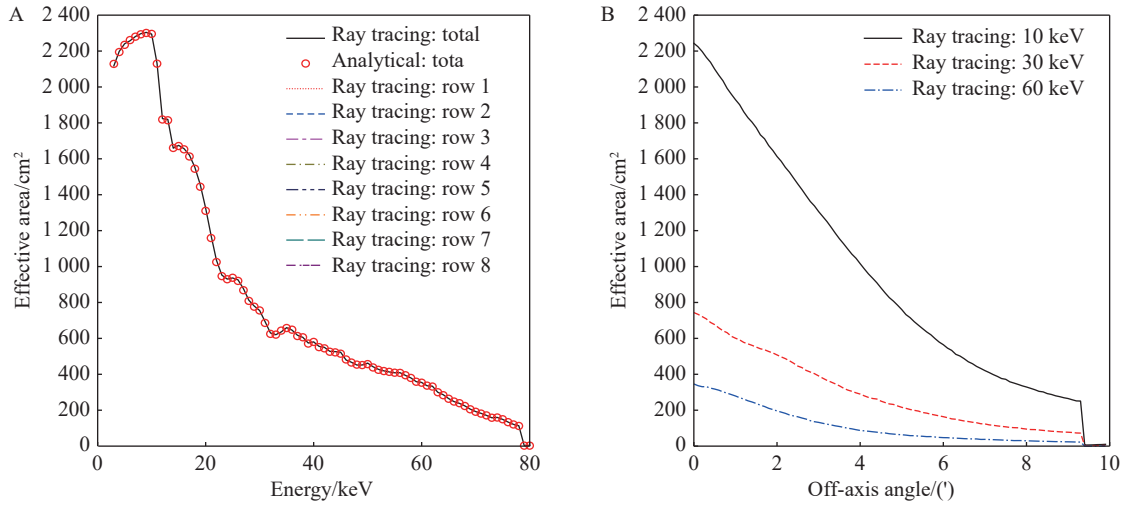


Fig. 11. On-axis effective area curves with an ideal surface profile, including individual contribution from each row (A). Effective area curves as a function of off-axis angle at different X-ray energies (B). The area to collect X-rays at the focal plane is 163 mm × 163 mm.

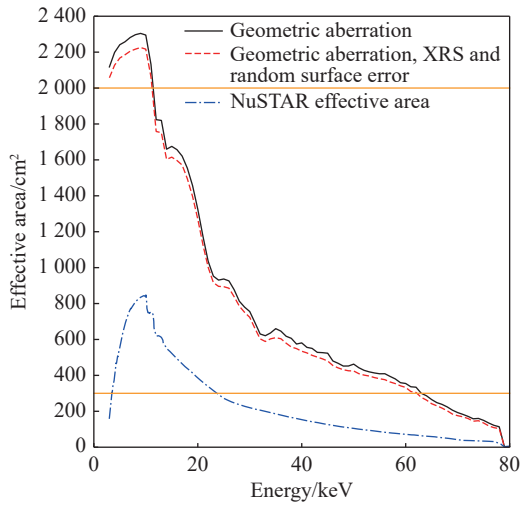


Fig. 12. On-axis effective area curves accounting for the XRS effect and random low-frequency surface errors. The effective area at 10 keV is 2216 cm² and the effective area at 60 keV is 333 cm². The orange solid lines represent scientific requirements of the on-axis effective area of 2000 cm² at 10 keV and 300 cm² at 60 keV. The effective area of NuSTAR is also plotted for comparison. The data are extracted from the NuSTAR Observatory Guide.

ror coating is a combination of W/Si and Pt/C multilayers, similar to that of NuSTAR. This fulfills the on-axis effective area requirements of 2000 cm² at 10 keV and 300 cm² at 60 keV, and provides a broad energy response between 3 keV and 78.4 keV.

To predict the mirror performance, we implement a mass modeling of the telescope in Geant4 using the ray-tracing algorithm. The complex geometry of the optics is built by replicating each pore to complete the mirror modules. The low-energy physics of X-rays (i.e., the reflection and scattering of X-rays on the optical surfaces) is implemented as boundary processes and incorporated into the standard physics list provided by Geant4. This can pre-

dict the angular resolution and effective area of the complete optics using metrological data, as input. Currently, a deficit of metrological data prohibits a proper input to the calculation. Instead, this work can provide precision and finishing requirements for optics manufacturing.

Our study demonstrates the feasibility of combining the techniques of multilayer coating and SPO for potential use in wideband X-ray telescopes, achieving good angular resolution and high throughput of X-ray focusing in a wide energy band from 3 keV to 78.4 keV. Such missions include the wideband X-ray Polarization Telescope, proposed in 2017 by the Institute of High Energy Physics, Chinese Academy of Sciences. Though alternative designs may exist, the geometries and parameters presented in this work provide a guide to the optics development of such missions. The methodology of this work can also be applied to areas such as optics design and performance prediction with metrological data.

ACKNOWLEDGEMENTS

We acknowledge the China National Space Administration program (D050102) and Youth Innovation Promotion Association CAS (2021011).

AUTHOR CONTRIBUTION

Liqiang Qi, Tianxiang Chen, and Zhengwei Li oversaw the overall technology of the optics system. Qianqing Yin managed the scientific requirements. Congzhan Liu supervised the wideband X-ray telescope project. Weichun Jiang contributed to the optics design. Lin Li was involved in calculating the reflectivity. All authors have reviewed and approved the final manuscript.

DECLARATION OF INTERESTS

The authors declare no competing interests.

REFERENCES

- [1] Wolter, H. 1952. Spiegelsysteme streifenden einfalls als abbildende optiken für Röntgenstrahlen. *Annalen der Physik*, **445**(1/2): 94–114. (in German)
- [2] Weisskopf, M. C., Tananbaum, H. D., Van Speybroeck, L. P., et al. 2000. Chandra X-ray Observatory (CXO): overview. In Proceedings of SPIE. 4012: 2–16.
- [3] Jansen, F., Lumb, D., Altieri, B., et al. 2001. XMM-Newton observatory-I. The spacecraft and operations. *Astronomy & Astrophysics*, **365**: L1–L6.
- [4] Predehl, P., Andritschke, R., Arefiev, V., et al. 2021. The eROSITA X-ray telescope on SRG. *Astronomy & Astrophysics*, **647**: A1.
- [5] Christensen, F. E., Hornstrup, A., Westergaard, N. J., et al. 1992. Graded d-spacing multilayer telescope for high-energy X-ray astronomy. In Proceedings of SPIE. 1546: 160–167.
- [6] Harrison, F. A., Craig, W. W., Christensen, F. E., et al. 2013. The nuclear spectroscopic telescope array (NuSTAR) high-energy X-ray mission. *The Astrophysical Journal*, **770**(2): 103.
- [7] Christensen, F. E., Jakobsen, A. C., Brejnholt, N. F., et al. 2011. Coatings for the NuSTAR mission. In Proceedings of SPIE. 8147: 298–316.
- [8] Barcons, X., Nandra, K., Barret, D., et al. 2015. Athena: the X-ray observatory to study the hot and energetic universe. *Journal of Physics: Conference Series*, **610**(1): 012008.
- [9] Beijersbergen, M., Kraft, S., Gunther, R., et al. 2004. Silicon pore optics: novel lightweight high-resolution X-ray optics developed for XEUS. In Proceedings of SPIE. 5488: 868–874.
- [10] Agostinelli, S., Allison, J., Amako, K., et al. 2003. GEANT4—a simulation toolkit. *Nuclear instruments and methods in physics research section A: Accelerators, Spectrometers, Detectors and Associated Equipment*, **506**(3): 250–303.
- [11] Nevot, L., Croce, P. 1980. Caractérisation des surfaces par réflexion rasante de rayons X Application à l'étude du polissage de quelques verres silicates. *Revue de Physique appliquée*, **15**(3): 761–779. (in France)
- [12] Parratt, L. G. 1954. Surface studies of solids by total reflection of X-rays. *Physical review*, **95**(2): 359.
- [13] Windt, D. L. 1998. IMD—Software for modeling the optical properties of multilayer films. *Computers in physics*, **12**(4): 360–370.
- [14] Mondal, B., Vadawale, S. V., Mithun, N. P., et al. 2021. DarpanX: A python package for modeling X-ray reflectivity of multilayer mirrors. *Astronomy and Computing*, **34**: 100446.
- [15] Joensen, K. D., Christensen, F. E., Schnopper, H. W., et al. 1993. Medium-sized grazing incidence high-energy x-ray telescopes employing continuously graded multilayers. In Proceedings of SPIE. 1736: 239–248.
- [16] Spiga, D., Christensen, F. E., Bavdaz, M., et al. 2016. Simulation and modeling of silicon pore optics for the ATHENA X-ray telescope. In Proceedings of SPIE. 9905: 1632–1655.
- [17] Collon, M. J., Günther, R., Ackermann, M., et al. 2008. Performance of silicon pore optics. In Proceedings of SPIE. 7011: 456–464.
- [18] Vacanti, G., Barrière, N., Bavdaz, M., et al. 2017. Predicting silicon pore optics. In Proceedings of SPIE. 10399: 131–136.
- [19] Qi, L. Q., Li, G., Xu, Y. P., et al. 2020. Geant4 simulation for the responses to X-rays and charged particles through the eXTP focusing mirrors. *Nuclear Instruments and Methods in Physics Research Section A: Accelerators, Spectrometers, Detectors and Associated Equipment*, **963**: 163702.
- [20] Qi, L. Q., Li, G., Ge, M. Y., et al. 2022. Implementation of the polarimetry focusing telescope array observation simulator on board the X-ray timing and polarimetry observatory. *The Astrophysical Journal*, **934**(2): 109.
- [21] Madsen, K. K., Harrison, F. A., Mao, P. H., et al. 2009. Optimizations of Pt/SiC and W/Si multilayers for the nuclear spectroscopic telescope array. In Proceedings of SPIE. 7437: 401–411.
- [22] Raimondi, L., Spiga, D. 2011. Point spread function of real Wolter-I X-ray mirrors: computation by means of the Huygens-Fresnel principle. In *Optics for EUV, X-Ray, and Gamma-Ray Astronomy V*, **8147**: 343–355.
- [23] Church, E., Takacs, P. 1986. The interpretation of glancing incidence scattering measurements. In Proceedings of SPIE. 640: 126–133.
- [24] Salmaso, B., Spiga, D., Canestrari, R., et al. 2013. X-ray scattering of periodic and graded multilayers: comparison of experiments to simulations from surface microroughness characterization. *Nuclear Instruments and Methods in Physics Research Section A: Accelerators, Spectrometers, Detectors and Associated Equipment*, **710**: 106–113.
- [25] Koglin, J. E., An, H. J., Barrière, N., et al. 2011. First results from the ground calibration of the NuSTAR flight optics. In Proceedings of SPIE. 8147: 81470J.